

BH α BAR : Big H α kinematical sample of BARred spiral galaxies - I. Fabry-Perot Observations of 21 galaxies

O. Hernandez^{1,2,*}, C. Carignan^{1,*}, P. Amram^{2,*}, L. Chemin¹ and O. Daigle^{1,*}

¹*Observatoire du mont Mégantic, LAE, Université de Montréal, C. P. 6128 succ. centre ville, Montréal, Québec, Canada H3C 3J7*

²*Observatoire Astronomique de Marseille Provence et LAM, 2 pl. Le Verrier, 13248 Marseille Cedex 04, France*

Accepted - 04/15/2005 . Received 01/30/2005

ABSTRACT

The H α gas kinematics of twenty-one representative barred spiral galaxies belonging to the *BH α BAR* sample is presented. The galaxies were observed with FANTOMM, a Fabry-Perot integral-field spectrometer, on three different telescopes. The 3D data cubes were processed through a robust pipeline with the aim of providing the most homogeneous and accurate dataset possible useful for further analysis. The data cubes were spatially binned to a constant signal-to-noise ratio, typically around 7. Maps of the monochromatic H α emission line and of the velocity field were generated and the kinematical parameters were derived for the whole sample using tilted-ring models. The photometrical and kinematical parameters (position angle of the major axis, inclination, systemic velocity and kinematical centre) are in relative good agreement, except maybe for the later-type spirals.

Key words: Keywords: galaxies: barred - galaxies: spiral - galaxies: kinematics and dynamics. Methods: observational. Techniques: radial velocities.

1 INTRODUCTION

The presence of a bar in disc galaxies seems to be a common feature. Bars have been recognized in galaxies since the time of Curtis (1918) and Hubble (1926). In the optical, roughly 30% of spiral galaxies are strongly barred (de Vaucouleurs 1963) while another 25% are weakly barred. Evidences that bars in spirals are more obvious in the near-infrared (NIR) than in the visible go back to Hackwell & Schweizer (1983). Recent surveys in the NIR have shown that up to 75% of high surface brightness galaxies may have a more or less strong bar (e.g. Knapen, Shlosman & Peletier 2000; Eskridge et al. 2000).

When present, such bars will introduce non-circular motions that should be seen in the radial velocity fields. Since the kinematics of barred spirals is different from the one of the more or less axisymmetric discs, it is important to model them properly if one wants to derive, as accurately as possible, the overall mass distribution. This distribution is directly derived from the knowledge of the circular velocities. Since the gas in axisymmetric galaxies is nearly on circular orbits, and its random motions are small compared with the rotation, its kinematics can be used to derive ro-

tation curves (RC). However, when a galaxy is barred, the gas response to the non-axisymmetric part of the potential cannot be neglected. Thus, a rotation curve derived without correcting for those non-circular motions cannot be said to represent the circular motions and be used to derive the mass distribution.

The presence of a bar is expected to leave signatures mainly in the central regions of the RCs Bosma 1981b; Athanassoula 1984; Combes & Gerin 1985; Schoenmakers, Franx, & de Zeeuw 1997; Athanassoula & Misiriotis 2002) which is the region where the free parameters of the mass models are really constrained (Blais-Ouellette et al. 1999, 2004; Blais-Ouellette, Amram & Carignan 2001). Indeed, the parameters of mass models are not constrained by the flat part but by the rising part of RCs.

Bars in galaxies have very different masses, lengths, axial ratios, colour distributions, gas content, pattern speeds, shapes and kinematics. The determination of the fundamental bar parameters is a delicate task. Even if the observational constraints are numerous, their determinations are rarely unambiguous. Difficulties come from the fact that

- the various galactic components (bar, disc, spiral arms, bulge, rings) are closely imbricated in disc galaxies: observations as well as models integrate the various components and one cannot observe them separately;
- 3D shapes in galaxies are observed projected on the

* Visiting Astronomer, Canada–France–Hawaii Telescope, operated by the National Research Council of Canada, the Centre National de la Recherche Scientifique de France, and the University of Hawaii.

plane of the sky and their deprojection is not unambiguous, particularly for barred galaxies;

- the parameters of bars depend on the luminous to dark matter ratio distribution, e.g. galaxies having initially the same disc and the same halo-to-disc mass ratio but different central haloes concentrations have very different properties (Athanasoula & Misiriotis, 2002).

Bars observed from 2D radial velocity fields contain a fraction of hidden information in tracing the total mass distribution (luminous & dark) and they may be directly compared to N-body + SPH simulations. Moreover, the signature of the bar can appear more significantly through the 2D gaseous velocity field (non symmetrical features due to gas chocs, SF regions of high density, i.e. related to the dissipative nature of the gas) than through the stellar one. So, 2D gaseous velocity fields give a valuable additional observational information that will help to disentangle the parameters of the bar.

For instance, the existence of a velocity gradient along the minor axis, in both the stellar and the gaseous 2D velocity fields, is not a very good criterion to pick out bars, while the angle between the kinematical major and minor axes and the twists of the isovelocity contours, are better criteria (Bosma 1981b).

Theoretical predictions from N-body simulations (e.g. Kormendy 1983; Lütticke et al. 2000; Athanasoula & Misiriotis 2002) may be summarized as follow.

When the position angle of the bar is:

- roughly parallel to the major axis, the isoveLOCITIES show a characteristic concentration towards the central region due to the fact that particle orbits are elongated along the bar and the velocity along an orbit is larger at pericentre than at apocentre;
- intermediate between the major and the minor axis positions angles, the velocity field shows the “Z” structure characteristic of barred galaxy velocity fields (see e.g. Peterson et al. 1978, for NGC 5383);
- roughly parallel to the minor axis, the velocity field shows a sizeable area of solid body rotation in the inner parts.

In the case of a dark halo more concentrated in the central regions of the galaxy, several of these features remain but some notable differences appear (Athanasoula & Misiriotis, 2002).

When the position angle of the bar is:

- roughly parallel to the major axis, the isoveLOCITIES show a strong pinching in the innermost region, on or near the bar minor axis;
- intermediate between the major and the minor axis positions angles, the “Z” shape of the velocity field is much more pronounced;
- roughly parallel to the minor axis, the innermost solid-body rotation part does not show strong differences but as we move away from the kinematical minor axis the isoveLOCITIES show a clear wavy pattern, indicating that the mean velocity is lower at the ends of the bar than right above or right below it.

This study is dedicated to the kinematics and the dy-

namics of barred galaxies. The aim will be to derive the most accurate velocity fields possible for a representative sample of barred galaxies in order to analyze their kinematics. The *BH α BAR* sample should provide the most homogeneous dataset on barred spiral galaxies to date. Once this database will be available, the following goal will be to model those galaxies, extract the non-circular component of the velocities and thus recover the circular motions and derive proper RCs. Only then will it be possible to model accurately their mass distributions.

This homogeneous study of the kinematics of twenty-one nearby barred spiral galaxies, based on the two-dimensional (2D) kinematics of the H α gas, is presented in this paper. Section 2 gives an overview of the observational campaign and presents the global properties of the *BH α BAR* sample while Section 3 discusses the data reduction and especially the adaptive binning that was performed. In Section 4, the kinematical parameters are derived and the FP maps are presented in Section 5. The conclusions can be found in Section 6 and an appendix presents a short observational description of the galaxies of the *BH α BAR* sample.

2 THE *BH α BAR* SAMPLE: OBSERVATIONS

2.1 The sample

The twenty-one galaxies of the *BH α BAR* sample were selected among northern ($\delta_{J2000} \geq +5.0$) nearby barred galaxies in de Vaucouleurs et al. (1991, hereafter the RC3) with systemic velocities $\leq 3000 \text{ km s}^{-1}$. Their optical sizes D_{25} were selected to take advantage of the specific field of view (FOV) of the three telescopes used (OmM: $D_{25} \geq 3.5'$; CFHT: $2.0' \leq D_{25} \leq 4.3'$ and OHP: $2.0' \leq D_{25} \leq 6.0'$).

To avoid problems related to disc opacity around H α wavelengths, galaxies with inclination $> 75^\circ$ have been discarded. The photometrical inclinations i were calculated using $q = b/a$, the ratio of the minor to the major axis, extracted from the value of R_{25} given in the RC3 and applying the following formula:

$$\cos^2 i = \frac{q^2 - q_0^2}{1 - q_0^2},$$

(Bottinelli et al. 1983) where q_0 is the intrinsic axial ratio of the disc (for an edge-on system). q_0 was not considered as a function of morphological types since the variation from its nominal value of $q_0 = 0.2$ is only significant for late type galaxies (types \geq Sd) which represent only 3 of the 21 galaxies in the sample. The selected galaxies reasonably sample the different morphological Hubble types, from SBB (or SABb) to SBdm (or SABdm) and have absolute magnitudes $M_B \leq -17$. The idea was to try to get a complete and homogeneous coverage of the Hubble sequence. However, due to their poor gas content, only one early type galaxy (SBB) was observed. At the other end of the sequence, only one Sdm was observed. Figure 1 gives an histogram of the sample.

The galaxies have also been chosen not to be in obvious interaction with close companions. To construct mass model and build the gravitational potential in future N-body models, galaxies with available HI data and surface photometry from the literature have been chosen: the photometry comes from Spitzer 3.6 μm and/or J,H,K $_s$ band high resolution

images (2MASS) or better ground images when available (e.g. Knapen et al. 2004 and 2003). Except for two cases which are Seyfert galaxies (NGC 6217 and NGC 7479), the galaxies have no nuclear activity. This confirmation of nuclear activity was not clear at the moment of the selection of the *BH α BAR* sample, so it was decided to keep them in the sample. This will be taken into account when, in further work, N-body coupled to SPH simulations will be done (forthcoming papers).

The global distribution versus morphological type and blue absolute magnitude (M_B) are shown in Fig. 1 and the basic information on the objects can be found in Table 1. The twenty-one velocity fields of the galaxies are mapped in Fig. 2.

2.2 Observing runs

The observations were obtained using FANTOMM¹ which is a permanent instrument on the OmM telescope, and a visitor instrument on various other telescopes. FANTOMM is a wide integral field spectrometer made of an image photon counting system (IPCS), a scanning Fabry Perot (FP) and an interference filter. The photocathode used has a high quantum efficiency ($\sim 30\%$ at H α). FANTOMM is coupled to the focal reducers of the telescopes used (see details in in Table 2).

The IPCS has a third generation photocathode with high quantum efficiency over a large wavelengths range (Hernandez et al. 2003 and Gach et al. 2002). This camera is very efficient to reach a good Signal-to-Noise ratio (S/N) for objects with very faint fluxes since, compared with CCDs, it has no read-out noise. Its multiplex mode also allows a rapid and efficient suppression of the OH sky lines since their variations can be averaged out. FANTOMM was used in its low spatial resolution mode of 512×512 pixels² (instead of 1024 pixels²).

The observations of the sample were spread over nine different observing runs over a three years period. Six runs were at the 1.6m of the Observatoire du mont Mégantic (OmM), one at the 1.93m of the Observatoire de Haute-Provence (OHP) and two at the the 3.6m of the Canada-France-Hawaii Telescope (CFHT). Various FP interferometers were used in order to fit the adequate spectral resolution. The interference orders vary from $p=765$ to $p=1162$, calculated for $\lambda_0=6562.78\text{\AA}$ (see Table 3).

All the calibrations were done using the same neon lamp (see below for more details on the data reduction). With the rapid analogic detector mode, calibrations were done in less than a minute. This allowed to perform as much calibrations as needed during the runs with very little overhead. A new bank of interference filters was also used covering a velocity range from 0 to 10,000 km s^{-1} (from 6562 \AA to 6785 \AA , with $\Delta\lambda \sim 15\text{\AA}$).

3 DATA REDUCTION

The reduction of the data cubes was performed using the package ADHOCw (Boulesteix 2004 and Amram et al. 1992) rewritten with large improvements under the IDL package (Daigle, Carignan & Hernandez 2005). The major improvements are the following:

- the elementary interferograms (elementary images obtained with an exposure time ranging from 10 to 15 seconds, depending on the sky transparency conditions and on the number of scanning steps) were corrected from sky fluctuations before summation;
- adaptive Hanning smoothing was performed in order to increase the S/N over the field;
- World Coordinates System (WCS) astrometry on the images was performed;
- strong and robust OH night sky lines removal was used;
- full automated and reproducible reduction and data analysis were performed.

3.1 Phase Calibration

Raw interferograms must be corrected to obtain data cubes sorted in wavelengths. This operation is called the “phase calibration” or wavelength calibration. Those calibrations are obtained by scanning the narrow Ne 6599 \AA line under the same conditions as the observations. Two phase calibrations are done, one before and the other after the exposure. Using the mean of the calibrations, a “phase map” is computed. It indicates the scanning step at which is observed the maximum of the interference pattern inside a given pixel. The FP formula below, giving the shape of the interference pattern on the detector as a function of the observed wavelength, allows us to find the observed Doppler-shifted wavelength λ at each point by comparison with

$$p\lambda = 2ne \cos \theta$$

where p is the interference order at λ_0 (here 6562.78 \AA), n the index of the medium, e the distance between the two plates of the FP and θ the incidence angle on the FP (angular distance on the sky). An uncertainty remains since the velocity is only known modulo the Free Spectral Range (column 10 in Table 3, note 11). This ambiguity is easily solved by using comparisons with long-slit spectroscopy or 21 cm HI line data to provide the zero point of the velocity scale. However, this means that when the redshift emission line of the galaxy is far from the calibration line, absolute values of the systemic velocity could be wrong (which is not a problem since we are mainly interested in relative velocities for our kinematical studies). In such cases, two ways are in development: a correction using the dispersion in the multilayer, semi reflective high Finesse coating, which is hard to model for high multilayers coating, or/and an absolute calibration (in development) done at the scanning wavelength. Nevertheless, the *relative* velocities with respect to the systemic velocity are very accurate, with an error of a fraction of a channel width ($< 3 \text{ km s}^{-1}$) over the whole field. In this study, systemic velocities of the sample, presented in Table 1, were taken directly from Tully (1988).

The signal measured along the scanning sequence was separated in two parts: (1) an almost constant level produced by the continuum light in a narrow passband around

¹ FANTOMM stands for Fabry-Perot of New Technology of the Observatoire du mont Mégantic (<http://www.astro.umontreal.ca/fantommm>).

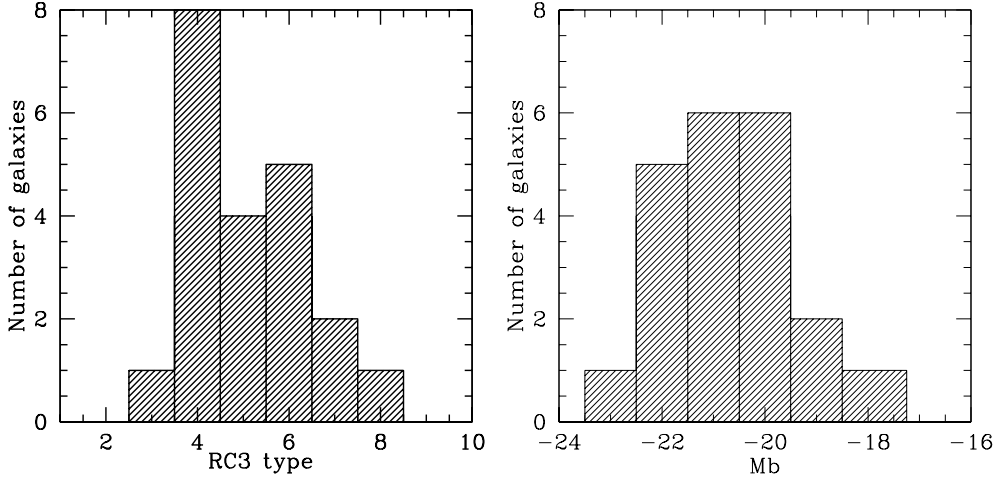


Figure 1. Histogram of the sample morphological types and M_B . **Left:** The type goes from SBb (type 3) to SBdm (type 8). **Right:** M_B varies from -17 to -23.

Table 1. Observational data for the *BH α BAR* sample.

Galaxy Name	α (J2000) hh mm ss	δ (J2000) ° ' "	Type RC3	D Mpc	$D_{25}^{b,i}$ "	$M_B^{b,i}$	$B_T^{b,i}$	$L_b^{b,i}$ "	PA_b °	V_{sys}	Image sources B	NIR
NGC 0925	02 27 16.8	+33 34 41	SAB(s)d	9.3 ^a	11.2	-20.0	10.6	56.5	112	554	XDSS	Spitzer
IC 0342	03 46 49.7	+68 05 45	SAB(rs)cd	3.9 ^b	27.9	-21.6	6.4	n/a ^c	32	32	XDSS	2Mass
NGC 1530	04 23 28.5	+75 17 50	SB(rs)b	36.6 ^b	4.8	-21.3	11.5	137.0 ^c	116	2460	XDSS	2Mass
NGC 2336	07 27 04.5	+80 10 41	SAB(r)bc	22.9 ^b	5.2	-22.1	11.1	72.8	5	2196	XDSS	2Mass
NGC 2403	07 36 54.5	+65 35 58	SAB(s)cd	4.2 ^a	21.4	-19.7	8.5	n/a ^c	n/a	132	XDSS	Spitzer
NGC 2903	09 32 09.7	+21 30 02	SB(s)bc	6.3 ^b	10.0	-19.8	9.13	143.4	26	554	XDSS	2Mass
NGC 3198	10 19 54.9	+45 33 09	SB(rs)c	14.5 ^a	7.8	-20.2	11.1	81.8	12	660	XDSS	Spitzer
NGC 3359	10 46 37.7	+63 13 22	SB(rs)c	19.2 ^b	7.2	-20.4	10.8	87.0	15	1013	XDSS	2Mass
NGC 3953	11 53 49.5	+52 19 39	SB(r)bc	17.0 ^b	5.2	-20.6	10.5	70.6	55	1054	XDSS	2Mass
NGC 3992	11 57 36.0	+53 22 28	SB(rs)bc	17.0 ^b	6.6	-20.7	10.4	136.5	37	1051	XDSS	2Mass
NGC 4236	12 16 42.1	+69 27 45	SB(s)dm	2.2 ^b	16.4	-17.3	9.5	170.7	143	2	XDSS	2Mass
NGC 4321	12 22 55.2	+15 49 23	SAB(s)bc	16.1 ^a	7.4	-22.1	10.0	53.4	107	1590	Kpn04	Spitzer
NGC 4535	12 34 20.3	+08 11 53	SAB(s)c	16.0 ^a	6.9	-22.0	10.6	70.0 ^c	45	1966	Kpn04	Kpn03
NGC 5371	13 55 40.6	+40 27 44	SAB(rs)bc	37.8 ^b	4.0	-21.6	11.3	47.2	97	2558	XDSS	2Mass
NGC 5457	14 03 12.5	+54 20 55	SAB(rs)cd	7.4 ^a	30.2	-22.7	8.3	86.5	84	231	XDSS	2Mass
NGC 5921	15 21 56.4	+05 04 11	SB(r)bc	25.2 ^b	4.9	-20.7	11.3	73.5	21	1480	XDSS	2Mass
NGC 5964	15 37 36.3	+05 58 28	SB(rs)d	24.7 ^b	4.0	-19.5	12.5	56.0 ^c	150	1447	Kpn04	Kpn03
NGC 6217	16 32 39.2	+78 11 53	(R)SB(rs)bc*	23.9 ^b	3.6	-20.2	11.7	68.8	153	1359	XDSS	2Mass
NGC 6946	20 34 52.0	+60 09 15	SAB(rs)cd	5.5 ^b	14.9	-20.8	7.92	34.5	166	46	Kpn04	Spitzer
NGC 7479	23 04 57.1	+12 19 18	SB(s)c*	32.4 ^b	3.8	-21.1	11.4	114.7	2	2382	XDSS	2Mass
NGC 7741	23 43 54.0	+26 04 32	SB(s)cd	12.3 ^b	3.8	-18.8	11.7	89.0	103	750	Kpn04	Kpn03

D : distances in Mpc

a - distances calculated from Cepheids (NGC 0925 - Silbermann et al. (1994), NGC 2403 - Freedman & Madore (1988), NGC 3198 - Kelson et al. (1999), NGC 4321 - Ferrarese et al. (1996), NGC 4535 - Macri et al. (1999), NGC 5457 - Kelson et al. (1996)).

b - distances are based on velocities, an assumed value of the Hubble Constant of $75 \text{ km s}^{-1} \text{ Mpc}^{-1}$, and the model that describes the velocity perturbations in the vicinity of the Virgo Cluster, c.f. Tully (1988).

$D_{25}^{b,i}$: optical diameter at the 25 magnitude/arcsecond² in B.

$M_B^{b,i}$: absolute magnitude in B.

$B_T^{b,i}$: apparent magnitude in B.

$L_b^{b,i}$: bar lengths from Martin 1995, all adjusted for the effects of projection and obscuration. ^c values not available in Martin (1995) are calculated from isophote fitting (except for NGC 1530 where the data are from Zurita et al. 2004).

PA_b : PA of the bar.

V_{sys} : systemic velocities provided by Tully (1988).

The symbol * refers to a nuclear activity.

Kpn04 refers to Knapen et al. 2004. Kpn03 refers to Knapen et al. 2003.

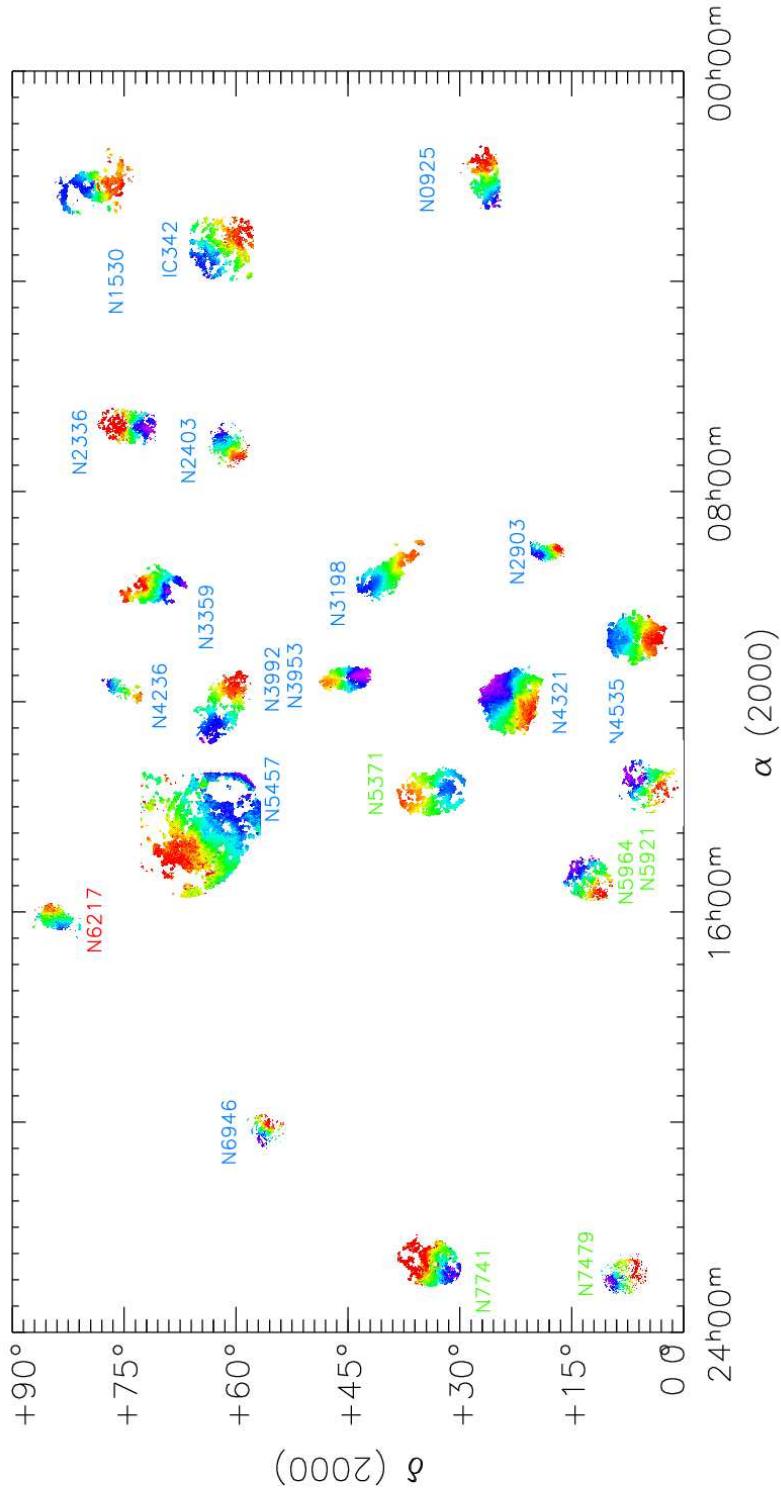


Figure 2. The *BH α BAR* sample sky coverage. The names in blue correspond to the observations done at the OmM, in green at the CFHT and in red at the OHP. The respective size of the galaxies given in *kpc* can be directly compared.

Table 2. FANTOMM characteristics on various telescopes.

Telescope Name	Focal Reducer	F/D	pixel size (")	FOV (')	FOV (vign.) (')
OmM	PANORAMIX	2.3	1.61	19.4	19.4
OHP	CIGALE	3.92	0.68	8.2	5.5
CFHT	MOS	2.96	0.48	5.8	3.9

F/D represents the ratio focal length over telescope diameter. The pixel size after binning is 2×2 , the original GaAs system providing 1024×1024 px². FOV is the diagonal Field Of View of the detector. FOV (vign.) represents the effective unvignetted FOV (whithout the vignetting due to the filter used).

Table 3. Journal of the Fabry Perot Observations.

Galaxy Name	Date	$\lambda_c^{(4)}$	Filter $\Delta\lambda^{(5)}$	T ⁽⁶⁾	Exposure		p ⁽⁹⁾	Fabry-Perot			Sampling	
					$t_{tot}^{(7)}$	$t_{ch}^{(8)}$		FSR ⁽¹⁰⁾	F^{11}	$R^{(12)}$	nch ⁽¹³⁾	stp ⁽¹⁴⁾
NGC 0925 ⁽¹⁾	02/11/02	6584	15	75	132	2.75	765	391.77	16	12240	48	0.18
IC 0342 ⁽¹⁾	02/11/03	6578	15	60	144	3	765	391.77	16	12240	48	0.18
NGC 1530 ⁽¹⁾	03/01/30	6622	15	70	240	5	899	333.36	20	17980	48	0.15
NGC 2336 ⁽¹⁾	02/11/10	6617	15	69	240	5	765	391.77	16	12240	48	0.18
NGC 2403 ⁽¹⁾	02/11/17	6569	10	50	120	3	765	391.77	14	10670	40	0.21
NGC 2903 ⁽¹⁾	03/02/08	6599	15	74	180	3.75	899	333.36	20	17980	48	0.15
NGC 3198 ⁽¹⁾	03/03/06	6584	15	75	260	5	899	333.36	23	20976	52	0.14
NGC 3359 ⁽¹⁾	01/11/17	6569	10	50	130	3.25	765	391.77	14	10670	40	0.21
NGC 3953 ⁽¹⁾	03/02/26	6599	15	74	273	5.25	899	333.36	23	20976	52	0.14
NGC 3992 ⁽¹⁾	03/02/27	6599	15	74	260	5	899	333.36	23	20976	52	0.14
NGC 4236 ⁽¹⁾	04/02/27	6578	15	60	182	3.5	899	333.36	23	20976	52	0.14
NGC 4321 ⁽¹⁾	03/02/25	6605	15	75	260	5	899	333.36	23	20976	52	0.14
NGC 4535 ⁽¹⁾	03/03/06	6617	15	69	156	3	899	333.36	23	20976	52	0.14
NGC 5371 ⁽²⁾	03/04/04	6622	15	70	88	1.83	899	333.36	16	17980	48	0.15
NGC 5457 ⁽¹⁾	03/02/28	6578	15	60	260	3.5	899	333.36	23	20976	52	0.14
NGC 5921 ⁽²⁾	03/04/09	6599	15	74	120	2.5	899	333.36	16	17980	48	0.15
NGC 5964 ⁽²⁾	03/04/08	6599	15	74	120	2.5	899	333.36	16	17980	48	0.15
NGC 6217 ⁽³⁾	01/10/17	6595	10	60	72	3	793	377.94	11	8722	24	0.34
NGC 6946 ⁽¹⁾	02/11/19	6569	10	50	120	2	765	391.77	14	10670	40	0.21
NGC 7479 ⁽²⁾	02/10/04	6617	15	69	60	6	1162	257.92	11	12782	24	0.23
NGC 7741 ⁽²⁾	02/10/06	6584	15	75	60	6	1162	257.92	11	12782	24	0.23

⁽¹⁾ OmM : Observatoire du mont Mégantic, Québec, Canada. 1.6m telescope.⁽²⁾ CFHT : Canada-France-Hawaii Telescope, Hawaii, USA. 3.6m telescope.⁽³⁾ OHP : Observatoire de Haute-Provence, France. 1.93m telescope.⁽⁴⁾ λ_c : filter central wavelength in Å⁽⁵⁾ $\Delta\lambda$ = FWHM : filter Full Width at Half Maximum in Å⁽⁶⁾ T : filter maximum transmission at λ_c ⁽⁷⁾ t_{tot} : total exposure time in minutes⁽⁸⁾ t_{ch} : exposure time per channel in minutes⁽⁹⁾ p : Fabry-Perot interference order at H α ⁽¹⁰⁾ FSR : Fabry-Perot Free Spectral Range (FSR) at H α in km s⁻¹⁽¹¹⁾ F : mean *Finesse* through the field of view⁽¹²⁾ R : resolution for a signal to noise ratio of 5 at the sample step⁽¹³⁾ nch : number of channels done by cycle in multiplex observations⁽¹⁴⁾ stp : wavelength step in Å

H α and (2) a varying part produced by the H α line (referred hereafter as the monochromatic map). After this calibration step, an adaptive binning was performed.

3.2 Adaptive binning and maps

A Hanning smoothing was performed on all the data cubes along the spectral axis. The Hanning smoothing can suppress the problems connected with the frequency response

(artifacts in the spectra caused by the sampling and the Fourier transform) of the spectra as a real function of finite length. The strong OH night sky lines passing through the filter were reconstructed into a cube and subtracted from the galaxy's spectrum (Daigle, Carignan & Hernandez 2005).

In order to increase the signal-to-noise ratio (S/N), an adaptive spatial smoothing, based on the 2D-Voronoi tessellations method (Cappellari & Copin 2002) was also applied to the 3D data cubes (Daigle, Carignan & Hernandez 2005)

before producing the monochromatic images and velocity fields. Each pixel was binned to reach a S/N of typically 5 to 10, depending on the observation conditions and the morphological type of the galaxy. This clever smoothing is effective in low S/N regions. First, in high S/N regions (S/N value superior to a fixed limit of 5, 7 or 10), the smoothing will not act and a bin is only one pixel. This will ensure to have the best spatial resolution possible in high S/N regions. This differs from the classical gaussian smoothing (Garrido et al. 2003, Zurita et al. 2004) where the kernel used will do the mix between a pixel and the adjacent one, and will cause a cross-pollution between the two regions. Second, for low S/N regions, pixels are binned until the S/N required is reached or the size of the resultant bin is reached (typically 30 px^2). This is very useful in interarm regions where the signal is dominated by the diffuse H α and not by HII regions. Thus, velocity maps have the best possible coverage without loosing any spatial resolution in the high S/N regions.

Finally, the intensity-weighted mean (barycentre) of the H α emission line profile was converted into wavelength and then in heliocentric radial velocity. Monochromatic images were obtained by integrating the H α profiles.

3.3 WCS astrometry

SAOIMAGE DS9 developed by the Smithsonian Astrophysical Observatory (Joye & Mandel 1999) has been used to find the correct astrometry of the monochromatic and H α images. KARMA (Gooch 1996) and its routine KPVSlice have been used to apply a co-ordinate system header to all images and data cubes. Systematic comparison between Ks band and XDSS Blue band images and the field stars in rough continuum images (with no adaptive binning) were made in order to find the correct WCS for each images. For the 21 galaxies of the BH α BAR sample, stars were easily found in rough continuum images.

4 DATA ANALYSIS

For each galaxy in the sample, Figures 5 to 25 provide: the blue band image (XDSS or Knapen et al. 2004), the NIR image (SPITZER 3.6 μm , Knapen et al. 2003 or 2MASS image), the H α monochromatic image, the velocity field and the Position-Velocity (PV) diagram.

Once the astrometry done on all the images and data cubes, the kinematical parameters were derived using GIPSY and KARMA.

The ROTCUR routine in the GIPSY package was used to find the kinematical parameters of the galaxies studied. ROTCUR (Begeman 1987) derives the kinematical parameters from the observed velocity field by fitting tilted-ring models. The observed velocities given in the velocity maps, V_{obs} , are obtained by solving the following equation

$$V_{\text{obs}} = V_{\text{sys}} + V_{\text{rot}}(R) \cos \theta \sin i + V_{\text{exp}}(R) \sin \theta \sin i$$

where V_{rot} is the rotation velocity, V_{exp} the expansion velocity, R and θ the polar coordinates in the plane of the galaxy and i the inclination. The same procedure was used for all the galaxies in the sample. The physical width of the rings is always the same: 4.83'' for the OmM, 2.04'' for the OHP and

1.44'' for the CFHT data; in order to have a good sampling of the signal.

Since all the galaxies in the BH α BAR sample are barred, it was decided to derive the kinematical parameters only in the axisymmetric part of the disc of the galaxy. This means that the central regions of the galaxy were systematically masked to avoid contamination from non circular motions due to the presence of the bar. Obviously, the solution will still be affected by the non-circular motions of the spiral disc itself. In order to determine the range of galactic radii to apply ROTCUR, the values of the deprojected bar lengths given by Martin (1995, and reported in Table 1, column 9) were used. For five galaxies not belonging to the ‘‘Martin’s’’ sample (IC 0342, NGC 1530, NGC 2403, NGC 4535 and NGC 5964), an ellipse fitting was done to determine an approximate bar length.

For each galaxy in the sample, a fit is first done simultaneously for the kinematical centre ($x_{\text{pos}}, y_{\text{pos}}$) and the systemic velocity V_{sys} , fixing the position angle $P.A.$ and the inclination i (using the photometrical values).

Secondly, by keeping V_{sys} and the kinematical centre fixed, $P.A.$ and i are allowed to vary over the same radius range and their mean values derived. It was decided to use the mean values of $P.A.$ and i since discs are rarely warped inside the optical radius; warps are mainly seen for $R > R_{\text{opt}}$. V_{rot} are then calculated keeping the 5 derived kinematical parameters, ($x_{\text{pos}}, y_{\text{pos}}$), V_{sys} , $P.A.$ and i fixed over the whole radius range. In all the fits, V_{exp} was not considered and fixed to zero. Finally, a 2D kinematical model for each galaxy of the BH α BAR sample was constructed using the VELFI routine of GIPSY and subtracted from the data to get a residual velocity map. This whole process was repeated until the mean and the dispersion of residuals were found to be minimal and close to zero and with a distribution as homogeneous as possible over the whole FOV.

To quantify the effect of masking the bar in the determination of the disc parameters, the residual maps (including the bar and masking it) were systematically compared. The means and the dispersions were computed for each residual map and for each galaxy. Results are presented in Table 4. The difference between the mean of the residual map in the disc part, using the model with the bar, and the mean of the residual map in the disc part, using the model avoiding the bar, are always close to zero (except for NGC7479 where there is a severe perturbation in the western arm). A difference is noticeable when comparing the dispersion of the residuals in the disc part, using the model with the bar and the dispersion of the residuals in the disc part, using the model avoiding the bar. The latter is always smaller than the former ($< 20 \text{ km s}^{-1}$). This suggests that the determination of the disc parameters is better when the bar region is avoided.

Once the most suitable 2D kinematical model was found, the KPVSlice routine of KARMA was used to derive a Position-Velocity (PV) diagram. This PV diagram is useful to check if the rotation curve derived from the whole 2-D velocity field is a good representation of the kinematics on the major axis. As the axisymmetrical models were derived using the disc region avoiding the bar, it is clear that strong non axisymmetrical motions can be seen in the bar region (e.g. NGC0925, NGC2903, NGC3198, NGC3359, NGC6217

Table 4. Analysis of the residuals

Galaxy	$\overline{m}_{idwb} - \overline{m}_{idab}$ (km s^{-1})	$\overline{\sigma}_{idwb}$ (km s^{-1})	$\overline{\sigma}_{idab}$ (km s^{-1})	Remarks
NGC 0925	+5.2	30.6	17.0	
IC 0342	n/a	n/a	n/a	bar not well defined
NGC 1530	+11.4	51.6	31.6	
NGC 2336	n/a	n/a	n/a	no H α in the bar region
NGC 2403	n/a	n/a	n/a	bar not well defined
NGC 2903	+1.0	20.3	19.8	
NGC 3198	+0.20	12.0	10.6	
NGC 3359	+1.0	21.5	12.9	
NGC 3953	+2.2	27.3	14.0	
NGC 3992	n/a	n/a	n/a	no H α in the bar region
NGC 4236	5.8	21.4	10.8	
NGC 4321	+0.8	15.6	13.8	
NGC 4535	+0.7	16.5	13.4	
NGC 5371	n/a	n/a	n/a	no H α in the bar region
NGC 5457	1.1	33.7	33.0	
NGC 5921	n/a	n/a	n/a	no H α in the bar region
NGC 5964	+2.8	25.9	16.7	
NGC 6217	+2.6	20.7	13.8	
NGC 6946	+1.1	18.5	13.3	
NGC 7479	+30.2	108.7	103.56	"broken arm" in the disc region
NGC 7741	+4.9	19.5	14.5	

\overline{m}_{idwb} : mean of the residual map in the disc part, using the model with the bar

\overline{m}_{idab} : mean of the residual map in the disc part, using the model avoiding the bar

$\overline{\sigma}_{idwb}$: dispersion of the residual map in the disc part, using the model with the bar

$\overline{\sigma}_{idab}$: dispersion of the residual map in the disc part, using the model avoiding the bar

and NGC7741). When the range of velocities in a galaxy was superior to the Free Spectral Range of the etalon used, the overall velocity range was distributed over two or three orders. In this case, data cubes have been replicated in the spectral dimension (twice or three times) to construct the PV diagrams. This is the case for NGC 7479, NGC 5371, NGC 4535, NGC 3992, NGC 3953, NGC 2903, NGC 2336 and NGC 1530.

Table 5 gives the results for the kinematical parameters fitting, compares with the photometrical data of the RC3 and indicates the shift between the photometrical and kinematical centres. Since, in the ROTCUR task, the kinematical value of *P.A.* is defined as the angle measured counterclockwise from the North to the receding side of the velocity field, it may thus differs from the RC3 value by 180°.

The agreement is good between the photometrical and the kinematical position angle, even for low inclination galaxies for which the photometrical position angle is difficult to determine accurately (Fig 3 left).

When comparing inclinations, noticeable discrepancies can be seen for two galaxies having a round shape (IC 0342 and NGC 4321) and a low photometrical inclination (<20°). The photometrical method used to determine the inclination, by fitting ellipses to the outer isophotes (or simply from the axis ratios), minimizes the inclination while the kinematical method is much less sensitive to this "face-on" effect. The shift between the position of the centre of the galaxy determined from the photometry and the kinematics is clearly a function of the morphological type of the galaxy (see Fig. 4). The strongest discrepancies occur for later type spirals for which the photometrical centre is not always easy to identify. The large value of the

offset when plotted in units of *arcsec* on Fig. 4 (left panel) shows that, for a large majority of galaxies, this difference may not be explained by seeing or spatial resolution effects. On the other hand, this offset is not statistically significant: NGC 2403, IC 0342, NGC 0925, and NGC 5457 have an offset of 1.17, 0.89, 0.67 and 0.30 kpc respectively while the bulk of 15 galaxies over 19 has an offset lower or equal to 0.1 kpc (Note : only 19 galaxies over 21 were studied because the determination of the photometrical centre for NGC 4236 and NGC 5964 was too hazardous).

Future N-body models coupled to a SPH code will help understand the gas behavior in a non axysymmetrical potential and may provide an explanation for such differences. The full analysis will be presented later.

5 CONCLUDING REMARKS AND FURTHER WORK.

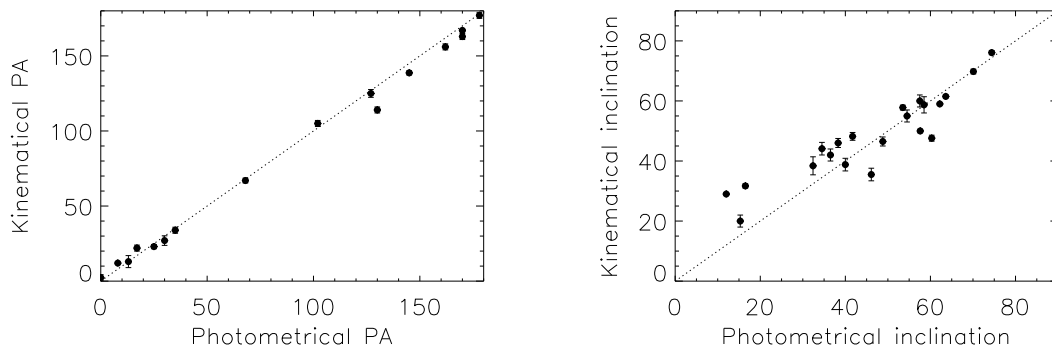
The 3D data presented in this paper are the results of a survey of the H α kinematics of nearby barred galaxies with the FP integral-field spectrometer FANTOMM. This study provides an homogenous sample of barred galaxies. The 3D data were processed through a robust reduction pipeline. An adaptive binning method has been used to achieve optimal spatial coverage and resolution at a given signal-to-noise ratio, typically around 7. High spatial and spectral resolutions H α monochromatic maps and velocity fields are presented. Bars' signatures in velocity fields and position-velocity diagrams, reveal strong non circular motions and thus provides observational constraints to extract the parameters of the

Table 5. HI, kinematical and photometrical position angles and inclinations. Offsets between kinematical and photometrical centres.

Galaxy name	HI		Ref.	Photometrical		H α kinematical		Offset from photo. centre	
	P.A. ($^{\circ}$)	Incl. ($^{\circ}$)		P.A. ($^{\circ}$)	Incl. ($^{\circ}$)	P.A. ($^{\circ}$)	Incl. ($^{\circ}$)	(arcsec)	(kpc)
NGC 0925	101.0 \pm 1.0*	58.5	1	102	57.6	105.0 \pm 1.0*	57.8 \pm 1.5	26.0	0.670
IC 0342	37 \pm 1.0	31 \pm 6.0	2	n/a	12.0	42.0 \pm 2.0	29.0 \pm 0.4	16.2	0.830
NGC 1530	n/a	58	3	n/a	60.3	5.0 \pm 1.0*	47.6 \pm 0.6	2.9	0.020
NGC 2336	n/a	59	4	178	58.5	177.0 \pm 1.3 \dagger	58.7 \pm 2.7	4.1	0.002
NGC 2403	124	61	5	127	57.5	125.0 \pm 1.0	60.0 \pm 2.0	25.4	1.167
NGC 2903	20*	61	4	17	63.6	22.0 \pm 1.0*	61.5 \pm 0.5	2.4	0.083
NGC 3198	36*	71	7	35	70.1	33.9 \pm 0.3*	69.8 \pm 0.8	8.4	0.105
NGC 3359	172 \dagger	51	8	170	54.5	167.0 \pm 2.0 \dagger	55.0 \pm 2.0	6.1	0.015
NGC 3953	11	58	9	13	62.2	13.0 \pm 0.8	59.0 \pm 0.4	6.5	0.086
NGC 3992	70 \pm 5*	57 \pm 1	10	68	53.5	67.0 \pm 1.0*	57.8 \pm 0.8	2.9	0.015
NGC 4236	163	75	11	162	74.4	156.1 \pm 1.6	76.1 \pm 0.7	55.5	0.498
NGC 4321	27 \pm 1 \dagger	27	12	30	16.5	27.0 \pm 1.0 \dagger	31.7 \pm 0.7	8.7	0.101
NGC 4535	3*	40	13	0	46.1	2.3 \pm 0.4*	35.0 \pm 2.0	3.6	0.057
NGC 5371	8	43	14	8	38.3	12.0 \pm 1.0	46.0 \pm 1.5	2.0	0.011
NGC 5457	49	18	15	n/a	15.3	53.0 \pm 1.0	20.0 \pm 2.0	17.7	0.297
NGC 5921	n/a	24	16	130	36.5	114.0 \pm 0.7	42.0 \pm 2.0	4.5	0.045
NGC 5964	144	41	17	145	40.0	138.7 \pm 0.7	38.8 \pm 2.1	15.0	1.130
NGC 6217	249	29	18	n/a	34.5	250.0 \pm 1.0	34.1 \pm 2.1	3.34	0.014
NGC 6946	240 \pm 1	38 \pm 5	19	n/a	32.4	239.0 \pm 1.0	38.4 \pm 3.0	8.2	0.163
NGC 7479	22	51	20	25	41.7	23.0 \pm 1.0*	48.2 \pm 1.3	7.2	0.060
NGC 7741	47	5	4	170	48.8	162.9 \pm 0.5*	46.5 \pm 1.5	3.9	0.023

P.A. = Position Angle of the major axis of the galaxy. \dagger indicates that P.A. = 180 $^{\circ}$ - kinematical P.A.. * indicates that P.A.=180 + kinematicalP.A.

References for HI data : 1 - Pisano, Wilcots & Elmegreen (1998); 2 - Crosthwaite, Turner & Ho. (2000); 3 - Teuben et al. (1993); 4 - WHISP data (van der Hulst, van Albada, & Sancisi 2001); 5 - Schaap, Sancisi, & Swaters (2000); 8- Ball (1986); 9 - Verheijen & Sancisi (2001); 10 - Bottema & Verheijen (2002); 11 - Shostak (1973); 12 - Knapen et al. (1993); 13- Guhathakurta et al. (1988); 14 - Zasov & Silchenko (1987); 15 - Bosma et al. (1981); 16 - Schulman et al. (1994); 17 - Hewitt et al. (1983); 18 - van Driel & Buta (1991); 19 - Carignan et al. (1990); 20 - Laine & Gottesman (1998)


Figure 3. Comparison between the kinematical and photometrical position angles and inclinations. Position angles are given modulo 180 $^{\circ}$. The dashed line represents the y=x equation.

bar and of the disc. Fine tuning of position angles and inclinations have been done. The kinematical parameters have been determined using a tilted-ring model, by taking into account only the axisymmetric part of the disc to avoid any kind of contamination due to non-circular motions from the bar (in the inner parts of the disc) or to a possible warp (in the outer parts).

The analysis of the sample shows that the photometrical and kinematical parameters (position angle of the major axis, inclination and centre) are in relative good agreement,

except maybe for the later-type spirals. Nevertheless, the determination of the kinematical parameters is more accurate than the photometrical one.

The main purpose of the paper is to provide and present an homogenous 3D data sample of nearby barred galaxies useful for further analysis. Velocity patterns of the bar(s) and of the spiral will be accurately determined using the Tremaine-Weinberg method (Tremaine & Weinberg 1984) on the H α velocity fields in two forthcoming papers. In Paper II the Tremaine-Weinberg method applied to the gaseous

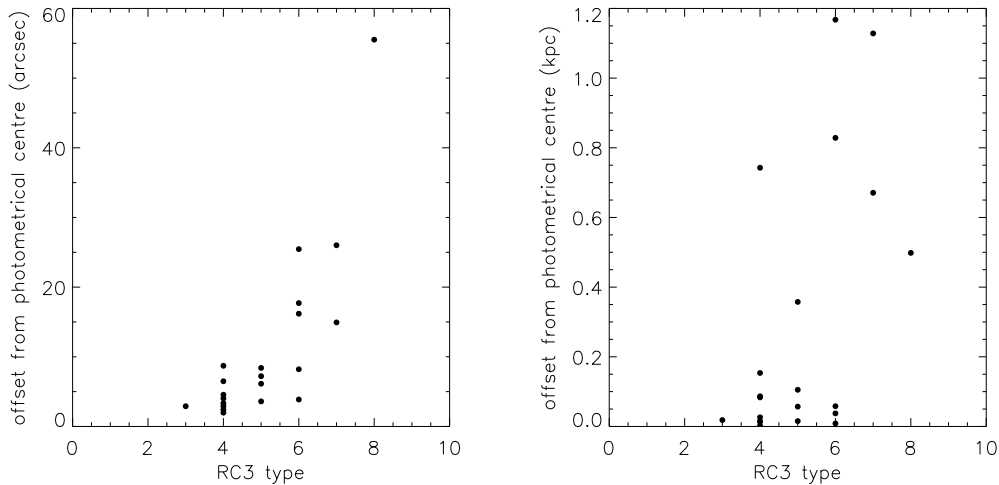


Figure 4. Left: Distance (in arcsec) between the photometrical and kinematical centres as a function of morphological type. The offsets are computed in the plane of the sky (not corrected for inclination). **Right:** Deprojected distance (in kpc) between the photometrical and kinematical centres as function of the morphological type. The offsets have been computed in the plane of the galaxy, using the position angles and the inclinations given in Table 5.

component will be discussed using numerical simulations and illustrated with the galaxy M100. In Paper III, the rest of the sample will be analyzed using this Tremaine-Weinberg method. In paper IV, the rotation curves will be derived, properly corrected for non-circular motions in order to retrieve the actual mass distributions. This will be achieved with N-body coupled with SPH simulations for each velocity fields of the $BH\alpha BAR$ sample. This kind of approach has been recently used by Pérez, Fux, & Freeman (2004). However, our study will differ in two major aspects. First, their comparison is relative to a small sample, whereas $BH\alpha BAR$ is homogeneous and well distributed over the Hubble sequence. Second, they only used long-slit data, whereas $H\alpha$ velocity fields and $H\alpha$ monochromatic images will be used to provide more accurate results avoiding, for example, the uncertainties on $P.A.$ and i present in 1D data. This will be the first step toward the determination of accurate mass models for barred spiral galaxies, until the time when full 2D mass models using the whole velocity fields will become available.

The whole data presented in the paper will be available for the community once paper II to IV will be published.

6 ACKNOWLEDGMENTS

We thank Chantal Balkowski for her help and support at the different stages of this work. We also thank Olivia Garrido, Jacques Boulesteix, Jean-Luc Gach, Philippe Balard and Olivier Boissin for their support. It is a pleasure to thank the OmM staff, in particular Bernard Malenfant and Ghislain Turcotte for their enthusiastic and competent support. Let us, also, acknowledge Pierre Martin and the CFHT team for their support at the top of the Mauna Kea. The FANTOMM project has been carried out by the Laboratoire d’Astrophysique Expérimentale (LAE) of the Université de Montréal using a grant from the Canadian Foundation for Innovation and the Ministère de l’Éducation du

Québec. This project made use of the LEDA database: <http://leda.univ-lyon1.fr/>. The Digitized Sky Surveys were produced at the Space Telescope Science Institute under U.S. Government grant NAG W-2166. The images of these surveys are based on photographic data obtained using the Oschin Schmidt Telescope on Palomar Mountain and the UK Schmidt Telescope.

High resolution images available on

www.astro.umontreal.ca/fantommm/bhabar/

Figure 5. NGC 0925. **Top left** : XDSS Blue Band image. **Top right** : 3.6 μm Spitzer image. **Middle left** : H α monochromatic image. **Middle right** : H α velocity field. **Bottom** : PV diagram. The H α velocity field and H α monochromatic image were spatially binned using an adaptive binning. The scale of the color used to represent the velocity is located to the right of the H α map. The PV diagram was obtained integrating over a slit of 3 pixels wide using the velocities of the model extracted from GIPSY and the data cube from the observations.

High resolution images available on

www.astro.umontreal.ca/fantommm/bhabar/

Figure 6. IC 0342. **Top left** : XDSS Blue Band image. **Top right** : 2Mass Ks-band image. **Middle left** : H α monochromatic image. **Middle right** : H α velocity field. **Bottom** : PV diagram.

High resolution images available on

www.astro.umontreal.ca/fantommm/bhabar/

Figure 7. NGC 1530. **Top left** : XDSS Blue Band image. **Top right** : 2Mass Ks-band image. **Middle left** : H α monochromatic image. **Middle right** : H α velocity field. **Bottom** : PV diagram.

High resolution images available on

www.astro.umontreal.ca/fantommm/bhabar/

Figure 8. NGC 2336. **Top left** : XDSS Blue Band image. **Top right** : 2Mass Ks-band image. **Middle left** : H α monochromatic image. **Middle right** : H α velocity field. **Bottom** : PV diagram.

High resolution images available on

www.astro.umontreal.ca/fantommm/bhabar/

Figure 9. NGC 2403. **Top left** : XDSS Blue Band image. **Top right** : 3.6 μm Spitzer image. **Middle left** : H α monochromatic image. **Middle right** : H α velocity field. **Bottom** : PV diagram.

High resolution images available on

www.astro.umontreal.ca/fantommm/bhabar/

Figure 10. NGC 2903. **Top left** : XDSS Blue Band image. **Top right** : 2Mass Ks band image. **Middle left** : H α monochromatic image. **Middle right** : H α velocity field. **Bottom** : PV diagram.

High resolution images available on

www.astro.umontreal.ca/fantommm/bhabar/

Figure 11. NGC 3198. **Top left** : XDSS Blue Band image. **Top right** : 3.6 μm Spitzer image. **Middle left** : H α monochromatic image. **Middle right** : H α velocity field. **Bottom** : PV diagram.

High resolution images available on

www.astro.umontreal.ca/fantommm/bhabar/

Figure 12. NGC 3359. **Top left** : XDSS Blue Band image. **Top right** : 2Mass Ks band image. **Middle left** : H α monochromatic image. **Middle right** : H α velocity field. **Bottom** : PV diagram.

High resolution images available on

www.astro.umontreal.ca/fantommm/bhabar/

Figure 13. NGC 3953. **Top left** : XDSS Blue Band image. **Top right** : 2Mass Ks band image. **Middle left** : H α monochromatic image. **Middle right** : H α velocity field. **Bottom** : PV diagram.

High resolution images available on

www.astro.umontreal.ca/fantommm/bhabar/

Figure 14. NGC 3992. **Top left** : XDSS Blue Band image. **Top right** : 2Mass Ks band image. **Middle left** : $H\alpha$ monochromatic image. **Middle right** : $H\alpha$ velocity field. **Bottom** : PV diagram.

High resolution images available on

www.astro.umontreal.ca/fantommm/bhabar/

Figure 15. NGC 4236. **Top left** : XDSS Blue Band image. **Top right** : 3.6 μm Spitzer image. **Middle left** : H α monochromatic image. **Middle right** : H α velocity field. **Bottom** : PV diagram.

High resolution images available on

www.astro.umontreal.ca/fantommm/bhabar/

Figure 16. NGC 4321. **Top left** : B band image from Knapen et al. 2004. **Top right** : 3.6 μm Spitzer image. **Middle left** : $\text{H}\alpha$ monochromatic image. **Middle right** : $\text{H}\alpha$ velocity field. **Bottom** : PV diagram.

High resolution images available on

www.astro.umontreal.ca/fantomm/bhabar/

Figure 17. NGC 4535. **Top left** : B band image from Knapen et al. 2004. **Top right** : Ks band image from Knapen et al. 2003. **Middle left** : H α monochromatic image. **Middle right** : H α velocity field. **Bottom** : PV diagram.

High resolution images available on

www.astro.umontreal.ca/fantommm/bhabar/

Figure 18. NGC 5371. **Top left** : B band image from Knapen et al. 2004. **Top right** : Ks band image from Knapen et al. 2003. **Middle left** : H α monochromatic image. **Middle right** : H α velocity field. **Bottom** : PV diagram.

High resolution images available on

www.astro.umontreal.ca/fantommm/bhabar/

Figure 19. NGC 5457. **Top left** : XDSS Blue Band image. **Top right** : 2Mass Ks band image. **Middle left** : H α monochromatic image. **Middle right** : H α velocity field. **Bottom** : PV diagram.

High resolution images available on

www.astro.umontreal.ca/fantommm/bhabar/

Figure 20. NGC 5921. **Top left** : XDSS Blue Band image. **Top right** : 2Mass Ks band image. **Middle left** : H α monochromatic image. **Middle right** : H α velocity field. **Bottom** : PV diagram.

High resolution images available on

www.astro.umontreal.ca/fantomm/bhabar/

Figure 21. NGC 5964. **Top left** : B band image from Knapen et al. 2004. **Top right** : Ks band image from Knapen et al. 2003. **Middle left** : H α monochromatic image. **Middle right** : H α velocity field. **Bottom** : PV diagram.

High resolution images available on

www.astro.umontreal.ca/fantommm/bhabar/

Figure 22. NGC 6217. **Top left** : XDSS Blue Band image. **Top right** : 2Mass Ks band image. **Middle left** : $H\alpha$ monochromatic image. **Middle right** : $H\alpha$ velocity field. **Bottom** : PV diagram.

High resolution images available on

www.astro.umontreal.ca/fantommm/bhabar/

Figure 23. NGC 6946. **Top left** : B band image from Knapen et al. 2004. **Top right** : 3.6 μm Spitzer image. **Top right** : 2Mass Ks band image. **Middle left** : H α monochromatic image. **Middle right** : H α velocity field. **Bottom** : PV diagram.

High resolution images available on

www.astro.umontreal.ca/fantommm/bhabar/

Figure 24. NGC 7479. **Top left** : XDSS Blue Band image. **Top right** : 2Mass Ks band image. **Middle left** : H α monochromatic image. **Middle right** : H α velocity field. **Bottom** : PV diagram.

High resolution images available on

www.astro.umontreal.ca/fantommm/bhabar/

Figure 25. NGC 7741. **Top left** : B band image from Knapen et al. 2004. **Top right** : Ks band image from Knapen et al. 2003. **Middle left** : H α monochromatic image. **Middle right** : H α velocity field. **Bottom** : PV diagram.

REFERENCES

- Amram, P., Le Coarer, E., Marcelin, M., Balkowski, C., Sullivan, W. T., & Cayatte, V. 1992, *A&APS*, 94, 175
- Artamonov B. P., Badan Y. Y., Bruyevich V. V., Gusev A. S. 1999, *ARep*, 43, 377
- Arsenault R., Roy J.-R., Boulesteix J. 1990, *A&A*, 234, 23
- Athanassoula E., 1984, *PhR*, 114, 321
- Athanassoula, E. & Misiriotis, A. 2002, *MNRAS*, 330, 35
- Ball R., 1986 *ApJ*, 307, 453
- Begeman, K. G. 1987, Ph.D. Thesis, Rijuniversiteit, Groningen
- Begeman K. G. 1989, *A&A*, 223, 47
- Blais-Ouellette, S., Amram, P., Carignan, C., & Swaters, R. 2004, *A&A*, 420, 147
- Blais-Ouellette, S., Amram, P., & Carignan, C. 2001, *AJ*, 121, 1952
- Blais-Ouellette, S., Carignan, C., Amram, P., & Côté, S. 1999, *AJ*, 118, 2123
- Bosma A. 1981a, *AJ*, 86, 1791
- Bosma A. 1981b, *AJ*, 86, 1825
- Bosma, A., Goss, W. M., & Allen, R. J. 1981, *A&A*, 93, 106
- Bottema R., Verheijen M. A. W. 2002, *A&A*, 388, 793
- Bottinelli L., Gouguenheim L., Paturel G., de Vaucouleurs G., 1983, *A&A*, 118, 4
- Boulesteix, J. 2004, www.oamp.fr/adhoc/adhoc.html
- Buta, R. & Crocker, D. A. 1993, *AJ*, 105, 1344
- Braine J., Combes F., Casoli F., Dupraz C., Gerin M., Klein U., Wielebinski R., Brouillet N. 1993, *A&AS*, 97, 887
- Canzian B. J., 1990, Ph.D. Thesis
- Canzian B., Allen R. J. 1997, *ApJ*, 479, 723
- Cappellari, M. & Copin, Y. 2002, in *ASP Conf. Ser. 282: Galaxies: the Third Dimension*, 515–+
- Carignan C., Charbonneau P., Boulanger F., Viallefond F. 1990, *A&A*, 234, 43
- Cayatte V., van Gorkom J. H., Balkowski C., Kotanyi C. 1990, *AJ*, 100, 604
- Cepa J., Beckman J. E. 1990, *A&AS*, 83, 211
- Combes F., Gerin M., 1985, *A&A*, 150, 327
- Corradi R. L. M., Boulesteix J., Bosma A., Amram P., Capaccioli M. 1991, *A&A*, 244, 27
- Crosthwaite, L. P., Turner, J. L., & Ho, P. T. P. 2000, *AJ*, 119, 1720
- Curtis, H. D. 1918, *Publ. Lick. Obs.*; Vol. 13; Page 45-54, 13, 45
- de Vaucouleurs G., 1963, *ApJS*, 8, 31
- de Vaucouleurs, G., de Vaucouleurs, A., Corwin, H. G., Buta, R. J., Paturel, G., & Fouque, P. 1991, Volume 1-3, XII, 2069 pp. 7 figs.. Springer-Verlag Berlin Heidelberg New York
- Daigle, O., Carignan, C., & Hernandez, O. 2005, in preparation
- Elmegreen B. G., Wilcots E., Pisano D. J. 1998, *ApJ*, 494, L37
- Eskridge P. B., et al. 2000, *AJ*, 119, 536
- Ferrarese L., et al., 1996, *ApJ*, 464, 568
- Fraternali F., Oosterloo T., Sancisi R., van Moorsel G. 2001, *ApJ*, 562, L47
- Freedman, W. L. & Madore, B. F. 1988, *ApJL*, 332, L63
- Gach, J.-L., Hernandez, O., Boulesteix, J., Amram, P., Boissin, O., Carignan, C., Garrido, O., Marcelin, M., Östlin, G., Plana, H., & Rampazzo, R. 2002, *PASP*, 114, 1043
- Garcia-Burillo S., Sempere M. J., Combes F., Neri R. 1998, *A&A*, 333, 864
- Garrido, O., Marcelin, M., Amram, P., Boissin, O. 2003, *A&A*, 399, 51
- Gooch, R. 1996, in *ASP Conf. Ser. 101: Astronomical Data Analysis Software and Systems V*, 80–+
- Gottesman S. T. 1982, *AJ*, 87, 751
- Guhathakurta, P., van Gorkom, J. H., Kotanyi, C. G., & Balkowski, C. 1988, *AJ*, 96, 851
- Hackwell J. A., Schweizer F. 1983, *ApJ*, 265, 643
- Helfer, T. T., Thornley, M. D., Regan, M. W., Wong, T., Sheth, K., Vogel, S. N., Blitz, L., & Bock, D. C.-J. 2003, *ApJS*, 145, 259
- Hernandez, O., Gach, J., Carignan, C., & Boulesteix, J. 2003, *SPIE*, 4841, 1472
- Hernandez, O., Wozniak, H., Carignan, C., Amram, P., Chemin, L. & Daigle O. 2005, submitted to *ApJ*
- Hewitt, J. N., Haynes, M. P., & Giovanelli, R. 1983, *AJ*, 88, 272
- Hubble, E. P. 1926, *ApJ*, 64, 321
- Joye, W. & Mandel, E. 1999, *ASP Conf. Ser. 172: Astronomical Data Analysis Software and Systems VIII*, 8, 429
- Kelson, D. D., et al. 1999, *ApJ*, 514, 614
- Kelson, D. D., et al. 1996, *ApJ*, 463, 26
- Knapen J. H., Cepa J., Beckman J. E., Soledad del Rio M., Pedlar A. 1993, *ApJ*, 416, 563
- Knapen J. H., Beckman J. E., Heller C. H., Shlosman I., de Jong R. S. 1995, *ApJ*, 454, 623
- Knapen J. H., Shlosman I., Heller C. H., Rand R. J., Beckman J. E., Rozas M. 2000, *ApJ*, 528, 219
- Knapen J. H., Shlosman I., Peletier R. F. 2000, *ApJ*, 529, 93
- Knapen J. H., de Jong R. S., Stedman S., Bramich D. M., 2003, *MNRAS*, 344, 527
- Knapen J. H., Stedman S., Bramich D. M., Folkes S. L., Bradley T. R., 2004, *A&A*, 426, 1135
- Kormendy, J. 1983, *ApJ*, 275, 529
- Laine S., Gottesman S. T. 1998, *MNRAS*, 297, 1041
- Lütticke, R., Dettmar, R.-J., & Pohlen, M. 2000, *A&A*, 362, 435
- Macri, L. M., et al. 1999, *ApJ*, 521, 155
- Marcelin M., Boulesteix J., Courtes G. 1982, *A&A*, 108, 134
- Marcelin M., Boulesteix J., Georgelin Y. 1983, *A&A*, 128, 140
- Martin, P. 1995, *AJ*, 109, 2428
- Martin P., Roy J. 1995, *ApJ*, 445, 161
- Pérez I., Fux R., Freeman K. 2004, *A&A*, 424, 799
- Peterson, C. J., Thonnard, N., Rubin, V. C., & Ford, W. K. 1978, *ApJ*, 219, 31
- Pisano D. J., Wilcots E. M., Elmegreen B. G. 1998, *AJ*, 115, 975
- Rand R. J. 1995, *AJ*, 109, 2444
- Rozas M., Zurita A., Beckman J. E. 2000, *A&A*, 354, 823
- Rozas M., Zurita A., Beckman J. E., Pérez D. 2000, *A&AS*, 142, 259
- Sakamoto K., Okumura S., Minezaki T., Kobayashi Y., Wada K. 1995, *AJ*, 110, 2075
- Schaap W. E., Sancisi R., Swaters R. A. 2000, *A&A*, 356,

L49

- Schoenmakers R. H. M., Franx M., de Zeeuw P. T. 1997, MNRAS, 292, 349
- Schulman, E., Bregman, J. N., & Roberts, M. S. 1994, ApJ, 423, 180
- Sérsic, J. L. 1973, PASP, 85, 103
- Shostak G. S. 1973, A&A, 24, 411
- Silbermann, N. A., et al. 1994, Bulletin of the American Astronomical Society, 26, 1353
- Sofue Y., Tomita A., Tutui Y., Honma M., Takeda Y. 1998, PASJ, 50, 427
- Teuben, P., Regan, M., Vogel, S., van der Hulst, T., & Wainscoat, R. 1993, Bulletin of the American Astronomical Society, 25, 1411
- Tremaine S., & Weinberg M. D., 1984, ApJ, 282, L5
- Tully, R. B. 1988, Journal of the British Astronomical Association, 98, 316
- van der Hulst J. M., van Albada T. S., Sancisi R., 2001, ASPC, 240, 451
- van Driel W., Buta R. J. 1991, A&A, 245, 7
- van Moorsel G. A. 1983, A&AS, 54, 19
- Verheijen M. A. W., Sancisi R. 2001, A&A, 370, 765
- Vogt N. P., Haynes M. P., Herter T., Giovanelli R. 2004, AJ, 127, 3273
- Wilke K., Möllenhoff C., Matthias M. 1999, A&A, 344, 787
- Wynn-Williams C. G., Becklin E. E. 1985, ApJ, 290, 108
- Zasov, A. V., & Silchenko, O. K. 1987, Soviet Astronomy Letters, 13, 186
- Zurita, A., Relaño, M., Beckman, J. E., & Knapen, J. H. 2004, AAP, 413, 73

APPENDIX A: DESCRIPTION OF THE INDIVIDUAL GALAXIES

A brief description of the structures observed in the H α velocity fields and monochromatic images of the BH α BAR sample is given in this section.

IC 0342: This large SAB(rs)cd nearby galaxy is nearly face-on so its photometrical position angle ($P.A.$) is uncertain. A strong difference between its kinematical and photometrical inclination is noted. Observations in CO and HI (Crosthwaite, Turner, & Ho 2000) suggest that its kinematical $P.A.$ is 37° . The kinematical data from CO, HI and H α are comparable. An H α spiral structure near the centre can be seen.

NGC 0925: This late type SBcd galaxy has a bright optical and H α bar and two bright patchy spiral arms beginning at the ends of the bar. Many HII regions lie along the bar. Photometrical and kinematical data agree. The PV diagram shows non axisymmetric motions near the centre. It is well studied in HI (Elmegreen, Wilcots, & Pisano 1998, Pisano, Wilcots, & Elmegreen 1998), in CO (Helfer et al. 2003) and in H α (Marcelin, Boulesteix, & Courtes 1982). It shows strong streaming motions.

NGC 1530: This strongly barred spiral galaxy has been extensively studied by Zurita et al. 2004. Here the FANTOMM observation provides much more details of the kinematics along the major axis due to its large FOV and high sensitivity. A nuclear spiral and a large velocity gradient are observed. In the V-band images, a nuclear bar

(Buta & Crocker 1993) with hot spots (Sérsic 1973) can be seen.

NGC 2336: NGC 2336 is an intermediate-type ringed barred spiral galaxy with a prominent bar. This galaxy shows a very regular morphological structure with no major asymmetries, except for the central regions where HI maps show a lack of gas in the centre (van Moorsel 1983). The H α monochromatic image suggests the same lack. The NW part of the disc has been cutoff by the wings of the interference filter. Although NGC 2336 belongs to an apparent pair of galaxies (together with IC 467) with a projected linear distance of 135 kpc, its undisturbed disc does not exhibit any distinct sign of recent interactions (Wilke, Möllenhoff, & Matthias 1999).

NGC 2403: This SABc galaxy shows amorphous spiral features. The H α velocity maps and the PV diagram show an almost rigid structure near the centre of the galaxy. Bright HII regions can be seen in the H α monochromatic image. It is not clear whether this galaxy is barred or not. According to Schoenmakers, Franx, & de Zeeuw (1997), their Fourier harmonic analysis of the HI velocity field shows that non-circular motions are not important in this galaxy. Moreover, Schaap, Sancisi, & Swaters (2000) stress that the thin hydrogen disc of NGC 2403 is surrounded by a vertically extended layer of HI that rotates slower than the disc. A complete modeling of the galaxy will provide more details on its structures. Fraternali et al. (2001) suggest that this anomalous HI component may be similar to a class of high velocity clouds observed in the Milky Way. In CO data, no molecular gas is detected (Helfer et al. 2003).

NGC 2903: This starburst galaxy shows several peaks of star formation in the circumnuclear region. These peculiar “hotspots” have been identified and described in different ways by various authors in H α (Marcelin, Boulesteix, & Georgelin 1983), in radio and in the infrared by Wynn-Williams & Becklin (1985). A strong velocity gradient can be seen along the bar in the velocity map. The PV diagram shows a clear step in the RC. This step-like structure could be related to its strong bar. The molecular gas, visible in CO observations (Helfer et al. 2003), follows the bar.

NGC 3198: This SB(rs)c galaxy has been extensively studied in HI (Bosma 1981a, Begeman 1989), FP H α (Corradi et al. 1991, Blais-Ouellette et al. 1999) and H α and [NII] long-slit spectroscopy (Sofue et al. 1998, Vogt et al. 2004). According to the PV diagram, non circular motions near the centre can be seen. A strong velocity gradient is also seen perpendicular to the bar major axis.

NGC 3359: NGC 3359 is a strongly barred galaxy. Its HII regions have been studied (Martin & Roy 1995) and cataloged (Rozas, Zurita, & Beckman 2000). The structure and kinematics of the HI were analyzed in detail by Gottesman (1982) and Ball (1986) showing a clumpy distribution and a low surface density within the annular zone of strong star formation, which can be explained as due to the effect of the bar sweeping up gas as it rotates. Analysis of the H α velocity map shows a disc with an axisymmetric rotation and also evidence of strong non circular motions as confirmed by Rozas et al. (2000). Analysis of the H α residual velocity map (not shown here) shows strong streaming motions in the spiral arms and a strong gradient of gas in the bar.

NGC 3953: One of the most massive spirals of the M81 group, it has been studied in HI by Verheijen & Sancisi (2001). It is rather poor in HI and the surface density drops near D_{25} . Moreover, in CO (Helfer et al. 2003), the gas seems to be located in a ring at the near end of the bar. In $H\alpha$, the same lack of gas in the centre can be seen, whereas the arms are well developed.

NGC 3992: This galaxy is the most massive spiral of the M81 group. Its HI distribution is regular. It has a prominent bar and very well defined spiral arms. It has a faint radial HI extension outside its stellar disc. There is a pronounced central HI hole in the gas distribution at exactly the radial extent of the bar (Bottema & Verheijen 2002), also visible in the $H\alpha$ emission line. Some $H\alpha$ can be seen toward the centre of the galaxy. It is not clear whether this feature could exist in HI because of the poor spatial resolution of the HI data measurements. Observations in CO (Helfer et al. 2003) stress the lack of molecular gas in the galaxy.

NGC 4236: This late type SBdm galaxy is seen nearly edge-on. Its kinematical inclination is 76° . The $H\alpha$ image shows that the HII regions are distributed along the bar, with two bright regions near the end of the bar. These features are also seen in HI (Shostak 1973). An extensive region of solid-body rotation coincides with the bar.

NGC 4321: This grand-design spiral galaxy has been frequently mapped in the $H\alpha$ emission line using high-resolution FP interferometry (Arsenault, Roy, & Boulesteix 1990, Cepa & Beckman 1990, Canzian & Allen 1997, Knapen et al. 2000), in the molecular CO emission-line (Canzian 1990, Sakamoto et al. 1995, Rand 1995, Garcia-Burillo et al. 1998, Helfer et al. 2003) and in the 21-cm HI emission-line (Cayatte et al. 1990, Knapen et al. 1993). The HI disc is almost totally confined within the optical one but with a slight lopsidedness towards the SW (Knapen et al. 1993). The HI, CO and $H\alpha$ velocity fields show kinematical disturbances such as streaming motions along the spiral arms and a central S-shape distortion of the iso-velocity contours along the bar axis. The circum-nuclear region (CNR) and shows the presence of an enhanced star formation region as a four-armed $H\alpha$ ring-like structure and a CO & $H\alpha$ spiral-like structure. Much more details can be found in Hernandez et al. 2005.

NGC 4535: With NGC 4321, this is another Virgo cluster galaxy with a known Cepheids distance (16.0 Mpc). It is not located in the main sub-structure of the cluster close to the core elliptical galaxy M87 but it lies in the southern extension related to M49. Although the $H\alpha$ morphology appears perturbed, with an obvious indication of multiple spiral arms (these features are even present in the NIR Ks image), its velocity field is regular. No HI was found in the central parts (Cayatte et al. 1990).

NGC 5371: In this galaxy, there is no evidence of $H\alpha$ emission in the centre.

NGC 5457: M101 is a large nearby galaxy. Observations of CO data (BIMA song, Helfer et al. 2003) show that the molecular gas is only distributed along the bar. In the $H\alpha$ image the gas is distributed over the whole field. Two large arms can be seen.

NGC 5921: This galaxy shows a ring like structure in both the $H\alpha$ and the XDSS blue images. The bar is not clearly seen in $H\alpha$ but many HII regions lie at the end of

the bar. The centre of galaxy is the host of a strong velocity gradient well defined in the $H\alpha$ velocity map. Nevertheless, no $H\alpha$ gas is present between the ring like structure and the centre.

NGC 5964: This galaxy shows strong HII regions distributed along its bar. Nevertheless, no strong velocity gradient can be seen in this direction.

NGC 6217: This galaxy presents a prominent bar, with an important region of stellar formation on it located at $10''$ in the southeastern direction from the galactic centre (Artamonov et al. 1999). The galactic centre reveals the presence of a different structural component, a ring. The size of the ring in $H\alpha$ observations is approximately of $43''$, which agrees with previous works in HI on this galaxy (van Driel & Buta 1991). The inner ring structure in the centre of the galaxy can be easily seen in the $H\alpha$ monochromatic image.

NGC 6946: According to HI studies (Carignan et al. 1990), the HI distribution is not symmetric but is more extended to the NE side. This feature is also seen in the $H\alpha$ emission map. The overall $H\alpha$ velocity map is regular but shows some non-circular motions near the centre, confirmed by the PV diagram. It has been recently observed in FP by (Blais-Ouellette et al. 2004) leading to the same conclusions. Once again the wide field of FANTOMM and its high sensitivity is clearly an advantage to obtain better $H\alpha$ velocity fields.

NGC 7479: This SB(s)c galaxy has been studied in HI by Laine & Gottesman (1998). The HI distribution shows considerable asymmetries and distortions in the outer disc. The HI and $H\alpha$ kinematics suggest that, while the global velocity field is fairly regular, a severe perturbation is present in the western spiral arm. There is also a strong velocity gradient along the bar confirmed in the PV diagram. The $H\alpha$ monochromatic image shows strong HII regions at one end of the bar.

NGC 7741: This galaxy shows a strong bar in the $H\alpha$, blue and Ks band images. Many HII regions are located along the bar. The velocity map clearly shows non-circular motions, whereas the velocity gradient is not too strong (compared with NGC 2903 for example).

This paper has been typeset from a $\text{\TeX}/\text{\LaTeX}$ file prepared by the author.